This article has been accepted for publication in IEEE Transactions on Power Systems. This is the author's version which has not been fully edited and content may change prior to final publication. Citation information: DOI 10.1109/TPWRS.2025.3597567

Beyond Monotonic Droop: Expanding Feasible Control Regions for Optimal Frequency Regulation

Hamad Alduaij*, *Student Member, IEEE*, Yang Weng*, *Senior Member, IEEE*, and Haoran Li*, *Member, IEEE*

***Abstract*—With the growing integration of Inverter-Based Resources (IBRs) for renewable energy, power grids are shifting towards hybrid generations. As the system becomes more complex, it is challenging to ensure optimal and safe control. Recent work shows how to achieve a conditional optimal control with stability ensured by pre-selecting one subclass of activation functions for control. However, we demonstrate that the subclass leads to a sub-optimal control policy for IBRs. To address this issue, we propose a method to enlarge the feasibility space for true optimality while preserving the Lyapunov stability. The key idea is to implement a conditional control strategy based on the damping. When IBRs observe that synchronous generators are on the way to stabilize the grid sufficiently, IBRs do not necessarily need to conduct droop control with monotonic function. In some cases, IBRs can conduct actions that more closely align with non-monotonic control to encourage renewable generations. This extends from monotonic to non-monotonic functional space. Moreover, based on Pontryagin's maximum principle, we prove that the extended region is sufficiently large to contain a globally optimal solution. By leveraging our activation function, which can be both monotonic and non-monotonic, our numerical results on various test cases show significant improvement compared to existing solutions.**

***Index Terms*—Inverter-Based Resources, Optimal Frequency Control, Sufficiently Large Feasible Control Region, Pontryagin's Maximum Principle, and Reinforcement Learning**

I. Introduction

To reduce the emission of carbon dioxide, renewable generations are increasingly introduced to the power grid via inverters [1]. If they are not well managed, power grids will suffer events [2]–[5]. Such shift renders the widely deployed linear-droop control less efficient, as such control models the generators as synchronous machines [6]–[9]. However, synchronous machine models can not adequately model intermittent generation with an inverter interface that reduces inertia and creates a nonlinear relationship in the control. Consequently, the synchronous machine-based linear control is far from optimum when we have Inverter-Based Resources (IBRs) [10]. With many countries setting ambitious zero-emission targets by 2050 [1], developing optimal control strategies is crucial for resilient and sustainable grids [11].

For the nonlinear control of the inverter, a direct approach is to approximate it using a linear time-varying control, where the slopes are adjusted based on changing operating conditions [9]. While such a method provides improvement over the linear control, they are often based on heuristic designs, e.g., a quadratic function over time, leading to non-optimal design [12]. For a more systematic approach, one can introduce a physics model partially to tune the droop gain adaptively, e.g., based on the wind turbine parameters [13]. Human expertise can also be used for fuzzy controllers [14]. Since we do not know physical behavior exactly [10], can we learn the behavior with guarantees of system stability and optimality via data-driven approaches?

To learn nonlinear controller policies, Reinforcement Learning (RL) has emerged as a promising method [15]–[17]. But, RL lacks inherent stability guarantees for critical infrastructure like power systems [18], [19]. So, the condition of Lyapunov stability was added as a constraint during RL training [20]–[22]. [23] finds a monotonically increasing function satisfies Lyapunov condition, similar to droop control. If the monotonic function is assumed, the paper shows how to regulate the frequency optimally conditioned on this assumption or selection. The objective chosen includes infinite norm to minimize maximum frequency deviations and L^2-norm for the average effect over the time horizon. Recurrent Neural Networks (RNNs) are used to not only ensure that the optimization considers all the temporal states but also to speed up the learning process. Recently, [24] extended the work by introducing communication among inverters, but the core idea is the same.

One problem of the method is the pre-selection of monotonic functions. There is no proof that non-monotonic functions can not ensure stability. Because of this, the optimization for frequency regulation does not consider a sufficiently large feasibility region for true optimality [25]. As a consequence, the control performance in [23] is sub-optimal. A natural question arises: Can we quantify a sufficiently large action region that contains the globally optimal solution? To answer the question, we look into the exactness of inequality when deriving the monotonic and non-monotonic relationship on the control function based on the swing equation.

There are two requirements for stability based on swing equation. One is the unique stable state. This is because converging to different operating points under the same condition indicates instability or undesirable operating conditions [26]. For this uniqueness, we observe that the damping values were ignored in [23], [24]. By incorporating damping, the control rule goes beyond the monotonic functional class, enlarging the potential region with stability. The second requirement for stability is the convergence of system states to an equilibrium point. Thus, we prove that a selected Lyapunov function is stable under the proposed non-monotonic control function with damping considered. For a proof, it is hard to find a direct analytical form. So, we employ the Pontryagin's maximum principle and Lagrangian multiplier to conduct a dual analysis. Such a detour makes us capable of showing that our solution

* All three authors contributed equally to this work.

in optimal frequency control is strictly better than the existing approaches with relaxed conditions. Specifically, we prove that the globally optimal solution lies in our quantified action region, and there is a high chance for the globally optimal solution to lie outside of the region in existing methods.

To train our controller, RNN is essential for considering all the past deviations, as the optimal frequency control can regulate the maximum overshoot and the average deviations over time. RNN as a computation graph also speeds up the learning process [23]. Within the recurrent structure, we further investigate the design of the RNN cell for target control functions. To achieve stable and optimal control functions, we devise a parallel structure for the RNN cell with nonlinear stacked ReLU functions. And, the weighted connections for the two coordinate blocks in the RNN cell are restricted into the maximal possible range, strictly guaranteed by the parameter clipping technology [27]–[29]. Finally, we generalize the problem setup on the objectives to show that the theorem holds broadly for different classes of cost functions. The optimal control strategy for different objectives shows distinct characteristics, monotonic or non-monotonic. For example, when the IBRs know that synchronous generators (SGs) will stabilize the system, IBRs will sometimes use non-monotonic control functions for achieving better performance in the objectives.

To validate our approach, we conduct simulations using the IEEE-39 bus system, a widely accepted benchmark for stability analysis [21], [23]. Our results demonstrate that the proposed controller outperforms previous designs across various state and action cost functions. For example, our design has lower overall cost values and converges faster. This improvement is particularly notable when the objective considers emission and fuel cost reductions, highlighting the controller's effectiveness in addressing key concerns in renewable-integrated power systems.

The rest of the paper is as follows. Section II provides mathematical modeling. Section III shows that past methods have a conservative action region, bringing non-optimal solutions. Section IV illustrates how the action region can be enlarged. Section V shows the extended region is sufficiently large: the globally optimal control lies within the region. Section VI presents numerical results, and Section VII concludes the paper.

II. Mathematical Modeling with Flexible Objective

Consider a n-bus power system with phase angles $\boldsymbol{\theta} = \{\theta_1, \cdots, \theta_n\}$ and the frequency deviations $\boldsymbol{\omega} = \{\omega_1, \cdots, \omega_n\}$. Based on $\dot{\theta}_i = \omega_i$, we can form the energy dissipation equation for controller designs. For example, Fig. 1 shows how to construct the swing equation when the mechanical power is converted to the electric power for a local bus i. For such a system, we have five different inputs in red lines that jointly create the inertia torque of the generator: $M_i\dot{\omega}_i$, where M_i is the inertia constant [30], [31].

The first one is the power from the mechanical part: $p_{m,i} = p_{g,i} - \frac{1}{R_i}\omega_i$, where $p_{g,i}$ is the governor set point or

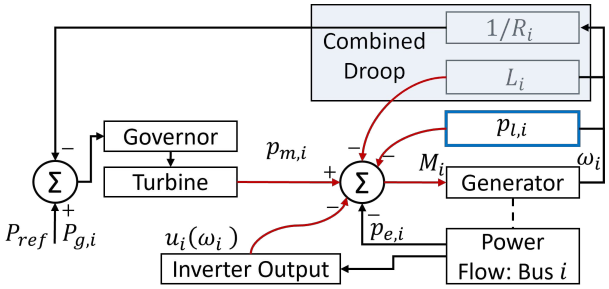

Figure 1: Frequency control loop at a generator with integrated inverter resources [30].

the scheduled mechanical power input to the generator. R_i is the droop characteristic of the governor and $\frac{1}{R_i}\omega_i$ represents the frequency-dependent component of the mechanical power. The second term $u_i(\omega_i)$ is the inverter output for frequency regulation like the droop control, so we give the negative sign the same as the sign in front of $\frac{1}{R_i}\omega_i$. The third term is load damping $L_i\omega_i$. The last two terms are the local load $p_{l,i}$ and the electrical power flow $p_{e,i} = \sum_{j=1}^{n} B_{ij}\sin(\theta_i - \theta_j)$. As they are using the power in some sense, the signs for them are negative. Therefore, we have

$$M_i\dot{\omega}_i = \left(p_{g,i} - \frac{1}{R_i}\omega_i\right) - u_i(\omega_i) - L_i\omega_i - p_{l,i} - p_{e,i} \quad (1)$$

$$= (p_{g,i} - p_{l,i}) - \left(\frac{1}{R_i} + L_i\right)\omega_i - p_{e,i} - u_i(\omega_i) \quad (2)$$

$$= p_i - D_i\omega_i - p_{e,i} - u_i(\omega_i), \quad (3)$$

where $p_i = p_{g,i} - p_{l,i}$ is the net power injection at bus i and $D_i = \frac{1}{R_i} + L_i$ is the combined droop coefficient for the SG and the load at bus i [32]. The combined droop is shown in the grey area in Fig. 1. In this paper, we will highlight that such a droop is useful for improving the feasibility region for control. Please note that a controller needs to satisfy not only the swing Eq. (3), but also the limits of power generation for IBRs at bus i during the dynamics, e.g., $u_i(w_i) \in [\underline{u}_i\overline{u}_i]$. What happens if there is no inverter on a bus? We set $\underline{u}_i = \overline{u}_i = 0$ for no control.

While one can use the swing Eq. (3) and inverter constraints to minimize the cost of frequency deviation, there is another constraint we need to enforce. The controller needs to have stability guarantees. For such a guarantee, we convert the swing Eq. (3) into an abstract form:

$$\dot{x}_i(t) = f(x_i(t), u_i(t)), \quad (4)$$

where we redefine the state in a vector form $x_i = (\theta_i, \omega_i)^T$. In such a form, $f(\cdot)$ is the dynamical function. Moreover, the system is stable if a Lyapunov function is a positive definite function $V(x)$. For example, if $V(x^*) = 0$, $V(x) > 0$ for all $x \in \mathcal{D}\backslash x^*$, and $\dot{V}(x) < 0$ for all $x \in \mathcal{D}\backslash x^*$ [33], [34], we have the Lyapunov stability at an equilibrium point x^*. In the rest of the paper, we also follow the classic setting for modeling the dynamics. We assume that (1) the voltage magnitude is 1 p.u., (2) the lines are lossless, and (3) the reactive powers are ignored [32]. We note that while simplified models are used for analysis, high-order models are used in simulations.

A. Flexible Objective Designs

In the past work, the objective is predefined with a fixed form. We generalize the objective in this subsection. Our objective includes two classes. One is the state cost, while the second class is the control cost [35]. This is based on the observation that most of the objectives can be modeled by these two classes, where the state cost evaluates the performance, e.g., frequency deviation and the control cost represents the efforts needed to have a good result [36]. Therefore, we define the optimization problem below.

$$\begin{aligned} \min_{\boldsymbol{u}} \sum_{i=1}^{n} (C_1(\omega_i) + \gamma C_2(u_i(\omega_i))) \\ \text{s.t.} \quad \boldsymbol{u}_i(\omega_i) \in \mathcal{U}_i, \end{aligned} \tag{5}$$

where $\mathcal{U}_i$ is the feasible region that admits stability for the swing equation dynamics, defined in Eq. (7), $C_1(\omega_i)$ denotes the cost for the deviations of controlled states, i.e., the frequency deviation. $C_2(u_i(\omega_i))$ is the cost for the control efforts, i.e., the change of active power generation for SGs and IBRs. For such two costs, $C_1(\omega_i)$ often employs a norm-based objective to measure the time-domain deviations of the frequency. L^2-norm accounts for averaged deviation, e.g., $\int_0^T (\omega_i(t))^2 dt$, where T is the total duration, while L^∞-norm looks into minimizing worst-case deviation, which is equivalent to the magnitude of frequency nadir in an under frequency disturbance.

For $C_2(u_i(\omega_i))$, we can design it to encourage renewable energy generation [37], [38], minimize fuel costs [39], reduce carbon emission cost [38], [40], and lower degradation cost due to heat and wear from changing the operating point [23]. Finally, the maximum rate of change of frequency (RoCoF) can also be augmented to C_1 to ensure system resilience [41]. All these can be captured in the general form $C_2(u_i(\omega_i)) = ||u_i(\omega_i)||^2 - \beta\omega_i$, where $\beta > 0$ is a weight to penalize the generation of the SG. When it is over-frequency, the objective will encourage the curtailment of SG over the curtailment of IBRs. When under-frequency, the objective tries to reward the increase of IBR generation and penalize SG generations.

Remark: We give further explanations for the objective $-\beta\omega_i$. This objective is proportional to the increase of the SG generation $-D_i\omega_i$ ($D_i > 0$), defined in Equations (3) in the paper. Namely, for different scenarios, this increase is minimized, and the curtailment of the SG generation is maximized. Specifically, we discuss the following scenarios.

- **Over-frequency scenario**. When $\omega_i > 0$, $-\beta\omega_i < 0$. Correspondingly, $-D_i\omega_i < 0$ and $-u_i(\omega_i) < 0$ are the SG and IBR generation curtailment, respectively. Minimizing the objectives in Equation (5) will (i) constrain the frequency deviation in $C_1(\omega_i)$, (ii) reduce the IBR generation curtailment in $||u_i(\omega_i)||^2$ by pushing $u_i(\omega_i) > 0$ towards 0, thus maximizing $-u_i(\omega_i)$, and (iii) increase the SG generation curtailment by minimizing the negative objectives $-\beta\omega_i$ and $-D_i\omega_i$. Note that this minimization will make $-D_i\omega_i$ towards a more negative value.
- **Under-frequency scenario**. When $\omega_i < 0$, $-\beta_i\omega_i > 0$. Correspondingly, $-D_i\omega_i > 0$ and $-u_i(\omega_i) > 0$ are the increase of the SG and IBR generation, respectively. Minimizing the objective in Equation (5) will (i) constrain the frequency deviation in $C_1(\omega_i)$, (ii) constrain the increase of IBR by minimizing $||u_i(\omega_i)||^2$ and pushing $u_i(\omega_i) < 0$ towards 0 which is important to respect actuator physical limits, and (iii) reduce the increase of the SG by minimizing the positive objectives $-\beta\omega_i$ and $-D_i\omega_i$. Although objective (ii) penalizes IBR production when it's under-frequency, it improves the transient responses by having a shorter settling time for the system and smoothens the controller's response. Moreover, we introduce objective (iii) so that the coordinate control is prioritized for reducing the increase of the SG. Then, by the power balance constraint, the IBR generation will increase. Notably, this prioritization doesn't exist for traditional optimal control with only objectives (i) and (ii).

B. Problem Definition

We can write the optimization below, with a general form for the objectives, to consider different needs, e.g., safety and economic benefits. Such a form makes our work applicable to a wide spectrum of OPF problems instead of a specific class [37]–[40].

$$\begin{aligned} \min_{\boldsymbol{u}} \sum_{i=1}^{n} (C_1(\omega_i) + \gamma C_2(u_i(\omega_i))) \\ \text{s.t.} \quad \boldsymbol{u}_i(\omega_i) \in \mathcal{U}_i, \end{aligned} \tag{6}$$

where $C_1(\omega_i)$ and $C_2(u_i(\omega_i))$ are defined above. Constraints of $\mathcal{U}_i = \{u_i | u_i \text{ is feasible}\}$ include the swing equation, the generation limits, and the stability condition.

$$\dot{\theta}_i = \omega_i, \tag{7a}$$

$$M_i\dot{\omega}_i = p_i - D_i\omega_i - \sum_{j=1}^{n} B_{ij}\sin(\theta_i - \theta_j) - u_i(\omega_i), \tag{7b}$$

$$\underline{u}_i \le u_i \le \overline{u}_i, \tag{7c}$$

$$u_i(\omega_i) \text{ is stabilizing to a unique equilibrium point.} \tag{7d}$$

III. Conservative Design Via Monotonically Increasing Functions

In this section, we will show that the past design is conservative, and we will illustrate how to enlarge the conservative design for a sufficiently large region to contain a globally optimal solution. Therefore, we can achieve significantly better performance in many scenarios. In general, two important properties are employed to evaluate the feasibility of the control actions: (1) Uniqueness. Feasible actions should control states to a unique equilibrium point, bringing guaranteed control results. (2) Stability. Feasible actions should be able to stabilize the state to the equilibrium point.

Conditions for uniqueness. Since (7d) requires $u_i(\omega_i)$ to stabilize to a unique equilibrium point, one needs to check what control property ensures a unique solution while satisfying (7b). Letting $\delta_i = \theta_i - \frac{1}{n}\sum_{j=1}^{n}\theta_j$ be the center-of-inertia coordinates [42], [43], we have $\theta_j = \delta_j - \frac{1}{n}\sum_{k=1}^{n}\theta_j$

by changing the subscript. Subtract the two terms, we have $\theta_i - \theta_j = \delta_i + \frac{1}{n}\sum_{k=1}^{n}\theta_j - \delta_j - \frac{1}{n}\sum_{k=1}^{n}\theta_j = \delta_i - \delta_j$. Therefore, we can rewrite the swing Eq. (7b) into

$$M_i\dot{\omega}_i = p_i - D_i\omega_i - \sum_{j=1}^{n} B_{ij}\sin(\delta_i - \delta_j) - u_i(\omega_i). \quad (8)$$

Taking the derivative of $\delta_i = \theta_i - \frac{1}{n}\sum_{j=1}^{n}\theta_j$ with respect to time, we have $\dot{\theta}_i = \omega_i - \frac{1}{n}\sum_{j=1}^{n}\omega_j$ at the equilibrium point. Moreover, there is zero dynamics, e.g., $\dot{\theta}_i = M_i\dot{\omega}_i = 0$. Therefore, for the local equilibrium point $(\boldsymbol{\delta}^*, \boldsymbol{\omega}^*)$ such that $\boldsymbol{\delta}^* = [\delta_1^*, \cdots, \delta_n^*]$ and $\boldsymbol{\omega}^* = [\omega_1^*, \cdots, \omega_n^*]$, we obtain

$$0 = \omega_i^* - \frac{1}{n}\sum_{j=1}^{n}\omega_j^*, \quad (9a)$$

$$0 = p_i - D_i\omega^* - u_i(\omega^*) - \sum_{j=1}^{n} B_{ij}\sin(\delta_i^* - \delta_j^*). \quad (9b)$$

To discuss the uniqueness of the equilibrium point, we must consider a certain state range because the state δ_i has cyclic patterns. For the angle range, since δ_i is computed as the center-of-inertia, we can safely conclude that the equilibrium point $\delta_i^* \in (-\pi/2, \pi/2)$ and $|\delta_i^* - \delta_j^*| \in [0, \pi/2)$, if buses i and j are connected. For the frequency range, it typically allows small variations around a nominal value [44]. Furthermore, at the unique equilibrium point, all buses must have a fixed and synchronized frequency ω^*. Therefore, $\omega_i^* = \omega^*$, for $\forall 1 \le i \le n$. Summing up (9a) for a lossless system leads to $\sum_{i=1}^{n} p_i = \sum_{i=1}^{n} u_i(\omega^*) + \omega^*\sum_{i=1}^{n} D_i$. Suppose there are two equilibrium points ω^* and $\hat{\omega}$. As the total power $\sum_{i=1}^{n} p_i$ does not change, we have $\sum_{i=1}^{n} p_i = \sum_{i=1}^{n} u_i(\omega^*) + \omega^*\sum_{i}^{n} D_i = \sum_{i=1}^{n} u_i(\hat{\omega}) + \hat{\omega}\sum_{i}^{n} D_i$. This leads to

$$\sum_{i=1}^{n}\frac{u_i(\omega^*) - u_i(\hat{\omega})}{\omega^* - \hat{\omega}} = -\sum_{i=1}^{n} D_i < 0. \quad (10)$$

[23] observes that the left hand side of Eq. (10) is positive, if $u_i(\omega)$ is monotonically increasing. But, this contradicts the negative sign on the right of (10), as the damping D_i is a non-negative physical term. Therefore, the monotonicity gives a sufficient condition for the design of $u_i(\omega)$ to verify the uniqueness of ω^*, needed in (7d). While a sufficient condition enables a unique outcome, there may exist another condition that creates better performance and preserves uniqueness and stability. Specifically, there is a significant and unexplored room for the coordination between SG and the IBR, encouraging a larger search room for the control of IBR, i.e., $u_i(\omega_i)$. We emphasize that this coordination does not require communication, as it is between the inverter and generator that share the same bus and frequency. Under the coordination, we can change the right-hand side of Eq. (10) to other negative values and still preserve the uniqueness.

Conditions for stability. To verify the stability of a Lyapunov controller, we need to find a Lyapunov function $V(x)$, satisfying the stability condition stated after Eq. (4). The condition is, if $V(x^*) = 0$, $V(x) > 0$ for all $x \in \mathcal{D} \setminus x^*$, and $\dot{V}(x) < 0$ for all $x \in \mathcal{D} \setminus x^*$. For constructing the Lyapunov function, typically, there are two parts summed together [45]. The first one is the mechanical energy, which can be expressed as $\frac{1}{2}\sum_{i=1}^{n} M_i(\omega_i - \omega_i^*)^2$. The second part is the electrical potential energy of the system, e.g., $W_p(\boldsymbol{\delta})$, representing the electrical power stored in the transmission network's inductors and capacitors [46].

$$V(\boldsymbol{\delta}, \boldsymbol{\omega}) = \frac{1}{2}\sum_{i=1}^{n} M_i(\omega_i - \omega_i^*)^2 + W_p(\boldsymbol{\delta}) \quad (11)$$

where $W_p(\boldsymbol{\delta}) = -\frac{1}{2}\sum_{i=1}^{n}\sum_{j=1}^{n} B_{ij}(cos(\theta_{ij}) - cos(\theta_{ij}^*)) - \sum_{i=1}^{n}\sum_{j=1}^{n} B_{ij}sin(\theta_{ij}^*)(\theta_i - \theta_i^*)$. In order to let the system be stable, we need $V(x) \ge 0, \dot{V}(x) \le 0$ according to the stability condition of Lyapunov function.

$$\dot{V}(x) = \frac{dV}{dt} = \sum_{i=1}^{n}\left(\frac{\partial V}{\partial \delta_i}\dot{\delta}_i + \frac{\partial V}{\partial \omega_i}\dot{\omega}_i\right). \quad (12)$$

We have $\sum_{i=1}^{n}\frac{\partial V}{\partial \delta_i}\dot{\delta}_i = 0$ based on our assumption of a lossless transmission assumption with voltages and currents are constant in a short time. In such a short time, the transmission network does not dissipate electric energy; hence the sum of total electrical energy stored in the system remains constant, making $\sum_{i=1}^{n}\frac{\partial V}{\partial \delta_i}\dot{\delta}_i = 0$. Also, since w_i on different buses will be the same after reaching the stability point, we replace w_i^* with w^* for compactness. Then, we have

$$\frac{dV}{dt} = \sum_{i=1}^{n}\frac{1}{2}(2M(\omega_i - \omega^*)\dot{\omega}_i) \quad (13)$$
$$= \sum_{i=1}^{n} D_i(\omega_i - \omega^*)^2 - \sum_{i=1}^{n}(\omega_i - \omega^*)(u_i(\omega_i) - u_i(\omega_i^*)).$$

We need the derivative $\frac{dV}{dt}$ to be negative for Lyapunov stability, as the negative derivative lets any points go to the equilibrium point only. One choice for strictly negative $\frac{dV}{dt}$ is to let each individual term be negative in (11). Therefore, we have the following inequality.

$$(\omega_i - \omega^*)(u_i(\omega_i) - u_i(\omega_i^*)) > (-D_i)\,(\omega_i - \omega^*)^2, \quad (14)$$

where we keep the controller u on the left hand side with a positive sign. Why is the region of the past method conservative under stability conditions? [23], [24] show that any control rule with $u(\omega_i)$ monotonically non-decreasing achieves local Lyapunov stability. However, we show that such a condition can be achieved with a more general condition. As ω^* is at the equilibrium point, when no more control should be dispatched, we set $u(\omega_i^*) = 0$. This leads to

$$\begin{cases} u_i(\omega_i) + D_i\omega_i > 0, & \text{if } \omega_i > 0, \\ u_i(\omega_i) + D\omega_i < 0, & \text{if } \omega_i < 0. \end{cases} \quad (15)$$

Eq. (15) brings a much relaxed condition for stability, compared to the monotonic requirement in [23], [24].

IV. Enlarge the Feasible Region for Control

In this section, we aim to investigate an enlarged action region with uniqueness and stability requirements. Strict derivations are given to show the region extension. Based on the derivation, we will show in the next section that

the enlarged region is sufficiently large to contain a globally optimal solution.

For uniqueness, we note that the control rule of SGs is typically linear with respect to frequency. This linear relationship is due to governors' mechanical limitations, such as the linearity of governor speed with power [47], the linearity of turbine power, and the valve position [30]. Therefore, we represent the contribution of the SG control by a linear droop gain $\alpha_i D_i$ to modify the control pattern of the SG, where $1 \geq \alpha_i \geq 0$ implies that the maximal possible frequency response coefficient for the SG is D_i. The value of α_i is determined by the modeling uncertainty in the SG and the desired robustness, as many SGs exhibit delays and nonlinear behavior, which can be bounded by α_i. Hence, in a coordination mode, the total controllable power between SG and IBR is $\tilde{u}_i(\omega_i, \alpha_i) = u_i(\omega_i) + \alpha_i D_i \omega_i$. Under this condition, we can now derive an equivalent form for the condition of the equilibrium point. Specifically, we have

$$\begin{aligned} 0 &= \omega_i^* - \frac{1}{n}\sum_{j=1}^{n} \omega_j^*, \\ 0 &= p_i - (1-\alpha_i) D_i \omega^* - \tilde{u}_i(\omega^*) - \sum_{j=1}^{n} B_{ij} \sin(\delta_i^* - \delta_j^*). \end{aligned} \tag{16}$$

Eq. set in (16) reduces to Eq. (9a), when $\alpha_i = 0$. This echoes our claims that the derivations from (8) to (15) lead to an overly conservative region. In particular, introducing α_i won't change the control law of the IBR and SG but brings convenient analyses for stability and the optimal control function design. First, for IBR, we emphasize that $\tilde{u}_i(\omega_i, \alpha_i)$ is only an intermediate variable. In the following derivation, we will prove that the stability can be achieved by making $\tilde{u}_i(\omega_i, \alpha_i)$ monotonic. However, the true control function for IBR, namely, $u_i(\omega_i)$ can be non-monotonic. The physical meaning is that the IBR control can consider the damping resources in the SG to gain more flexibility, which is better than previous methods. Second, the droop control for the SG is $D_i\omega_i$ but not $(1-\alpha_i)D_i\omega_i$ to satisfy the swing equation dynamics. In general, our theory reveals that as long as there is damping ($D_i > 0$) in the SG, IBR can make use of these resources to behave non-monotonically but still achieve stability. More importantly, non-monotonic property is preferred to encourage the generation of IBRs. Finally, we note that similar to previous work [21], [23], [48] in the design phase, we omit the upper and lower bounds of the SGs. However, in simulations we implement $\underline{u}_{SG} \leq u_{SG} \leq \overline{u}_{SG}$.

In the next lemma, we will prove that Eq. (16) provides an **relaxed sufficient condition** for the uniqueness of the equilibrium point.

Lemma 1. *Let $\tilde{u}_i(\omega_i, \alpha_i) = u_i(\omega_i) + \alpha_i D_i \omega_i$. Assume that the angles at equilibrium satisfy $|\delta_i^* - \delta_j^*| \in [0, \pi/2)$, if bus i and j are connected. Then, there exists a unique equilibrium point $(\boldsymbol{\delta}^*, \boldsymbol{\omega}^*)$ if for $1 \geq \alpha_i \geq 0$, $\tilde{u}_i(\omega_i, \alpha_i)$ is monotonically increasing with respect to a local frequency deviation ω_i.*

Proof. Eq. (16) is equivalent to

$$\sum_{i=1}^{n} p_i = \sum_{i=1}^{n} \tilde{u}_i(\omega^*, \alpha_i) + (1-\alpha_i)\omega^* \sum_{i=1}^{n} D_i. \tag{17}$$

Consequently, Eq. (17) is the sufficient and necessary condition for the equilibrium point. Then, we only need to investigate the equivalent condition for the uniqueness. To prove the sufficiency of the condition, we assume that $\tilde{u}_i(\omega_i, \alpha_i)$ is monotonically increasing. Assuming there are two equilibrium points ω^* and $\hat{\omega}$ for (17) leads to

$$\begin{aligned} &\sum_{i=1}^{n} \tilde{u}_i(\omega^*, \alpha_i) + (1-\alpha_i)\omega^* \sum_{i}^{n} D_i \\ =&\sum_{i=1}^{n} \tilde{u}_i(\hat{\omega}, \alpha_i) + (1-\alpha_i)\hat{\omega} \sum_{i}^{n} D_i. \end{aligned} \tag{18}$$

which is equivalent to:

$$\sum_{i=1}^{n} \frac{\tilde{u}_i(\omega^*, \alpha_i) - \tilde{u}_i(\hat{\omega}, \alpha_i)}{\omega^* - \hat{\omega}} = -(1-\alpha_i)\sum_{i=1}^{n} D_i \leq 0. \tag{19}$$

Then, the left hand side of Eq. (19) is positive, which brings a contradiction.

□

Rather than the sufficient condition in [23] with $\alpha_i = 0$, our case considers $\alpha_i \in [0, 1]$ for a relaxed sufficient condition to support the uniqueness of the equilibrium point. Subsequently, we need to prove that this condition always implies the stability of the system. Thus, this condition can satisfy all constraints in Eq. (7). To be more specific, we propose the following theorem.

Theorem 1. *Consider the unique equilibrium point $(\boldsymbol{\delta}^*, \boldsymbol{\omega}^*)$ defined in Lemma 1 with a region of attraction $\mathcal{D}_i = \{(\boldsymbol{\delta}, \boldsymbol{\omega}) || \delta_i - \delta_j | \in [0, \pi/2),$ buses i and j are connected.$\}$. For the monotonically increasing function $\tilde{u}_i(\omega_i, \alpha_i)$ with $1 \geq \alpha_i \geq 0$, $(\boldsymbol{\delta}^*, \boldsymbol{\omega}^*)$ is locally and exponentially stable.*

Proof. First, by Lemma 1, we have established that $\tilde{u}_i(\omega_i, \alpha_i) = u_i(\omega_i) + \alpha_i D_i \omega_i$ being monotonically increasing ensures a unique equilibrium point $(\boldsymbol{\delta}^*, \boldsymbol{\omega}^*)$ satisfying Eq. (17).

If $u_i(\omega_i)$ is monotonically increasing (i.e., $\alpha_i = 0$), local asymptotic stability was shown in (11)-(15) and exponential stability can be demonstrated following the example of [23], where the Lyapunov derivative $\dot{V}$ is bounded using the quadratic form and applying the Rayleigh-Ritz theorem establish $\dot{V} \leq -cV$ proving exponential stability.

For the relaxed condition where we only assume $\tilde{u}_i(\omega_i, \alpha_i)$ is monotonically increasing with $\alpha_i \in [0, 1]$, we follow the same stability analysis. The key requirement is that $\tilde{u}_i(\omega_i, \alpha_i) - \tilde{u}_i(\omega^*, \alpha_i)$ and $\omega_i - \omega_i^*$ have the same sign.

This condition is precisely what Lemma 1 guarantees through the monotonicity of $\tilde{u}_i(\omega_i, \alpha_i)$, as shown in Eq. (19) where:

$$\frac{\tilde{u}_i(\omega^*, \alpha_i) - \tilde{u}_i(\hat{\omega}, \alpha_i)}{\omega^* - \hat{\omega}} > 0.$$

Therefore, the same Lyapunov-based stability proof from [23] applies directly to our case with the relaxed condition,

establishing local and exponential stability of the unique equilibrium point. □

Combining Lemma 1 and Theorem 1, we can conclude that the monotonic property of $\tilde{u}_i(\omega_i, \alpha_i)$ brings an extended region of $\mathcal{U}_i$, compared to the state-of-the-art [23], [24]. To further quantify the region, we give the following corollary.

Corollary 1. *Assume that the feasible range for the monotonically increasing function $\tilde{u}_i(\omega_i, \alpha_i)$ is $[\underline{\tilde{u}}_i(\omega_i), \overline{\tilde{u}}_i(\omega_i)]$, then, $\mathcal{U}_i = [\underline{\tilde{u}}_i(\omega_i) - D_i\omega_i, \underline{\tilde{u}}_i(\omega_i)] \cap [\underline{u}_i, \overline{u}_i]$.*

By Corollary 1, $u_i(\omega_i)$ can be non-monotonic since the lower bound is $\underline{\tilde{u}}_i(\omega_i) - D_i\omega_i$ with an extra negative slope $-D_i$. This allows the optimization of flexible objectives such as carbon emissions and renewable curtailment.

V. Globally Optimal Control with a Sufficiently Large Region

A. Optimality via the Enlarged Region

The last section proves that the proposed region is much larger than the feasible region for control from previous methods with stability guarantees. However, the question remains whether the identified area of $\mathcal{U}_i$ is sufficiently large to contain the globally optimal solution. In this subsection, we prove the following two properties: (1) there exists the globally optimal control action in $\mathcal{U}_i$ and (2) in many cases, the globally optimal control action lies outside of the region identified in the state-of-the-art [23], [24].

Theorem 2. *For the proposed optimization in* (5)*, the following properties hold:*

- *There exists an **globally** optimal solution $u_i^*(\omega_i)$ in the identified region of $\mathcal{U}_i$ in Corollary 1.*
- *Within a time interval, if $\tilde{u}_i^* + \frac{\beta}{2} - \frac{\omega_i}{\gamma} - \alpha_i D_i \dot{\omega}_i > 0$ is not monotonically increasing with respect to ω_i. Namely, the optimal solution is outside of the range in existing work [23].*

Proof. To prove the result directly, we need to find $\frac{du_i^*}{d\omega_i}$ to indicate the increasing or decreasing trends for the optimal policy function. However, this is hard to compute due to the fact that there is no explicit expression, and the function $u_i^*(\omega_i)$ is estimated by a neural network. Therefore, we adopt an alternative approach, where we use Lagrangian dual to calculate the derivative in the dual space. After such a calculation, we will return to the original space to calculate $\frac{du_i^*}{d\omega_i}$. However, the analytical framework of Lagrangian dual and Pontryagin's maximum principle only provides the necessary conditions for a locally optimal solution. We note that the objectives proposed in II-A are convex with respect to the action $\boldsymbol{u}_i$. This implies that the investigated optimality is for a globally optimal solution. In general, we will provide the following steps for proof.

Step 1. Introduce Lagrangian analysis. To introduce Lagrangian analytical framework for optimal control problem, we employ Pontryagin's maximum principle [49]. Specifically, for the optimization in bus i, we introduce the time-varying Lagrangian multiplier for the ODE constraints, leading to a Hamiltonian function over $[0, T]$

$$\begin{aligned} H &= C_1(\omega_i) + \gamma C_2(u_i(\omega_i)) \\ &+ \lambda_i\big(p_i - \sum_j B_{ij}\sin(\delta_i - \delta_j) - (1-\alpha_i)D_i\omega_i - \tilde{u}_i(\omega_i)\big). \end{aligned} \tag{20}$$

According to the first-order condition for the optimal solution, we have:

$$\begin{aligned} &\frac{\partial H}{\partial \tilde{u}_i}|_{\tilde{u}_i=\tilde{u}_i^*} = \gamma \frac{dC_2}{d\tilde{u}_i}|_{\tilde{u}_i=\tilde{u}_i^*} - \lambda_i \\ &= \gamma \frac{d\big[[\tilde{u}_i(\omega_i,\alpha_i)]^2 - 2\alpha_i D_i\omega_i\tilde{u}_i(\omega_i,\alpha_i) + (\alpha_i D_i\omega_i)^2\big]}{d\tilde{u}_i(\omega_i,\alpha_i)}|_{\tilde{u}_i=\tilde{u}_i^*} \\ &- \lambda_i \\ &= 2\gamma\tilde{u}_i^*(\omega_i,\alpha_i) - 2\gamma\alpha_i D_i\omega_i - \lambda_i = 0 \\ &\implies \tilde{u}_i^* = \frac{\lambda_i}{2\gamma} + \alpha_i D_i\omega_i. \end{aligned} \tag{21}$$

Step 2. Compute dual state evolution. According to Eq. (21), to compute $\tilde{u}_i^*$, we need to calculate the evolution of the multiplier λ_i, i.e., the dual state. By Hamiltonian functions, we have:

$$\begin{aligned} \dot{\lambda} = -\frac{\partial H}{\partial \omega_i} =& \gamma\beta - \frac{dC_1}{d\omega_i} + [\lambda_i - 2\gamma\tilde{u}_i + 2\gamma\alpha_i D_i\omega_i]\frac{d\tilde{u}_i}{d\omega_i} \\ &+ 2\gamma\alpha_i D_i(\tilde{u}_i - \alpha_i D_i\omega_i) + \lambda_i(1-\alpha_i)D_i. \end{aligned} \tag{22}$$

Step 3. Return to the analysis of the original state. By Equations (21) and (22), we have:

$$\dot{\tilde{u}}_i|_{\tilde{u}_i=\tilde{u}_i^*} = \frac{d\tilde{u}_i}{d\omega_i}\dot{\omega}_i|_{\tilde{u}_i=\tilde{u}_i^*} = \tilde{u}_i^* + \frac{\beta}{2} - \frac{1}{2\gamma}\frac{dC_1}{d\omega_i}. \tag{23}$$

To further investigate the sign of $\frac{d\tilde{u}_i}{d\omega_i}$, since the L_2 and L_∞ have similar effects, we utilize L_2 norm for analysis, which brings well-defined gradients. Hence, $\frac{dC_1}{d\omega_i} = 2\omega_i$. Since $\frac{1}{2\gamma}$ is large as frequency control is prioritized over action cost when it's over-frequency, the Right-Hand-Side (RHS) of Eq. (23) is negative. When it's under-frequency, the RHS of Eq. (23) is positive. Then, we need to figure out the sign of $\dot{\omega}_i$ so that we can determine if $\frac{d\tilde{u}_i}{d\omega_i}$ is positive or negative.

The theorem discusses the property of the globally optimal solution u_i^* and $\tilde{u}_i^*$, which is the ideal solution as the Pontryagin maximum principle is derived based on a centralized full state-feedback controller. We use the analysis to study how such a controller would act and use it as a design guide for the neural network-based local controller. In this ideal case, once there is an over-frequency (under-frequency) scenario, the controller will immediately take action to push the deviation to 0. Thus, for the over-frequency (under-frequency) case, the globally optimal controller will make $\dot{\omega}_i < 0$ ($\dot{\omega}_i > 0$). In other words, the ideal controller will never enable $\dot{\omega}_i > 0$ ($\dot{\omega}_i < 0$) to enlarge the frequency deviations. We note that for our controller, the power imbalances are not measurable. Therefore, we can only consider them as disturbance with zero means in the optimization problem, which allows us to design a controller that attempts to enforce $\dot{\omega} < 0$ ($\dot{\omega} > 0$) whenever $\omega > 0$ ($\omega < 0$). Hence, $\frac{d\tilde{u}_i}{d\omega_i} > 0$ always hold, bringing a monotonic relationship between $\tilde{u}_i$ and ω_i.

For the second property, we have $\tilde{u}_i(\omega_i, \alpha_i) = u_i(\omega_i) + \alpha_i D_i \omega_i$. Therefore,

$$\frac{du_i^*}{d\omega_i} = \frac{\tilde{u}_i^* + \frac{\beta}{2} - \frac{\omega_i}{\gamma}}{\dot{\omega}_i} - \alpha_i D_i. \tag{24}$$

This suggests that for the over-frequency scenario, when $\tilde{u}_i^* + \frac{\beta}{2} - \frac{\omega_i}{\gamma} - \alpha_i D_i \dot{\omega}_i > 0$, u_i^* is not monotonically increasing. This condition can happen because $\dot{\omega}_i < 0$ and the decreasing rate can be large.

□

The conditions specified in Theorem 2 are critical due to the following reasons: (1) the term $|\dot{\omega}_i|$ is relatively large to quickly stabilize the frequency and (2) the hyper-parameters γ and β in the objective design are relatively large, which encourages the curtailment of SG generations. More specifically, when the system is over-frequency, all the hyper-parameters mentioned in reason (2) promote the cost penalization for SG generations. As a result, the curtailment function for IBR generation, $u_i(\omega_i)$, does not necessarily increase as the frequency ω_i rises. Conversely, the curtailment function for SG generation, $D\omega_i$, is monotonically increasing with ω_i.

B. Non-monotonic Controller to Learn the IBR Control with A Sufficiently Large Feasible Region

To solve the optimization and provide a nonlinear controller, we a introduce neural network based controller $\tilde{u}_i(\omega_i, \alpha_i; \Theta)$ as a universal approximator to learn the nonlinear control policy for the RL agent to make decisions, where Θ represents the network's weights. According to Section III, we need to: (a) limit $\alpha_i \in [0, 1]$, (b) restrict the parameterized controller, $\tilde{u}_i(\omega_i, \alpha_i; \Theta)$ to be monotonically increasing with respect to ω_i, (c) set $\tilde{u}_i(0, \alpha_i; \Theta) = 0$, and (d) enable saturation constraints in Eq. (7) are satisfied. Then, gradient descent will search local optimal solutions of Θ in the sufficiently large region $\mathcal{U}_i$. To achieve these goals, we introduce the following critical techniques for the controller, we revisit some definition in [23], and adapt the designs into our framework.

1) Structural Design with a Parameter Clip to Ensure $\alpha_i \in [0, 1]$: For requirement (a), recall that $u_i(\omega_i; \Theta) = \tilde{u}_i(\omega_i, \alpha_i; \Theta) - \alpha_i D_i \omega_i$. So, we propose a structural design that includes a neural network $\tilde{u}_i(\omega_i, \alpha; \Theta)$ plus a linear layer $\alpha_i D_i \omega_i$. To make sure that the constraint always holds when updating weights, we employ parameter clipping [28], [29]. Specifically, for the i^{th} training iteration, clipping requires a mapping

$$\alpha_i \leftarrow \max(\min(\alpha_i, 1), 0). \tag{25}$$

2) Non-Monotonic Stacking ReLU to Gain Monotonic Property for $\tilde{u}_i(\omega_i, \alpha; \Theta)$: For requirements (b) and (c), we design a non-monotonic stacking ReLU function: $\tilde{u}_i(\omega_i, \alpha; \Theta)$ is a one-layer neural network. When $\omega_i > 0$, $f_i^+(\omega_i) = \boldsymbol{q}_i \sigma(\mathbf{1}\omega_i + \boldsymbol{b}_i)$, where $\boldsymbol{q}_i, \boldsymbol{b}_i \in \mathbb{R}^m$ are the weight and bias vectors, respectively. m is the number of neurons in the layer. $\sigma(x) = \max(x, 0)$ is the ReLU function. We can make $f_i^+(\omega_i)$ monotonically increasing by setting $\sum_{j=1}^{l} q_i^j \geq 0, \forall l = 1, 2, \cdots, m$, $b_i^1 = 0$, and $b_i^l \leq b_i^{l-1}, \forall l = 2, 3, \cdots, m$. The proofs of the monotonic property can be found in [23]. Similarly, when $\omega_i < 0$, $f_i^-(\omega_i)$ is defined. The defined $f_i^+(\omega_i)$ and $f_i^-(\omega_i)$ together make sure that $\tilde{u}_i(\omega_i, \alpha; \Theta)$ is monotonically increasing when $\omega_i \in \mathbb{R}$ and passes the origin.

3) Another ReLU Outside to Satisfy Saturation Constraint: For requirement (d), we utilize the ReLU again to make sure the final output satisfy the saturation constraint:

$$\begin{aligned} u_i(\omega_i) =& \overline{u}_i - \sigma\big(\overline{u}_i - (f_i^+(\omega_i) + f_i^-(\omega_i) - \alpha_i D_i \omega_i)\big) \\ &+ \sigma\big(\underline{u}_i - (f_i^+(\omega_i) + f_i^-(\omega_i) - \alpha_i D_i \omega_i)\big). \end{aligned} \tag{26}$$

C. RNN-Based Controller Training

In this section, we show how to train the proposed controller. First, we discretize the system to apply reinforcement learning based approaches. The discrete dynamics is obtained using a fixed time step Δt. At each step $k = 0, 1, \ldots, K$, we approximate

$$\theta_i(k+1) = \theta_i(k) + \Delta t\, \omega_i(k), \tag{27}$$

$$\begin{aligned} \omega_i(k+1) =& \frac{1}{M}\omega_i(k) - \frac{\Delta t}{M}\sum_{j=1}^{n} B_{ij} sin(\theta_i - \theta_j) + \frac{1}{p_i}\Delta t \\ &+ (1 - \frac{D\Delta t}{M})\omega(k) - \frac{\Delta t}{M} u(\omega_i(k); \Theta), \end{aligned} \tag{28}$$

where $(\theta_i[k], \omega_i[k])$ are the angle and frequency at step k and $u_i(\omega_i[k])$ is the inverter control.

To learn the weights and biases of the neural-network-based controller, we embed our controller in an RNN structure unrolled in time and trained via a gradient-based reinforcement learning (RL) approach. The purpose of the RNN structure is to provide a computationally efficient way to propagate the gradients through automatic differentiation [23]. We note that the RNN framework does not add additional control nor affect the stability as it is constrained to embed the system dynamics in (28) to facilitate learning $u(\omega_i(k); \Theta)$ [23]. The pseudocode is summarized in Algorithm 1, which uses mini-batches of simulated trajectories and updates parameters by backpropagating the loss through the unrolled RNN cells.

a) Forward Pass (RNN Unrolling): As discussed in Section IV, each bus i applies a control law

$$u_i(\omega_i; \Theta) = \overline{u}_i - \sigma\big(\overline{u}_i - \tilde{u}_i(\omega_i, \alpha_i; \Theta)\big) + \sigma\big(\underline{u}_i - \tilde{u}_i(\omega_i, \alpha_i; \Theta)\big),$$

where

$$\tilde{u}_i(\omega_i, \alpha_i; \Theta) = f_i^+(\omega_i) + f_i^-(\omega_i) - \alpha_i D_i \omega_i.$$

To account for time-coupling, we treat (θ_i, ω_i) as the hidden "cell state." At each stage k, the RNN cell (controller) receives $(\theta_i(k), \omega_i(k))$ as input and outputs the control $u_i(k)$. The power-system equations (7) then update the states to $(\theta_i(k+1), \omega_i(k+1))$, which are passed to the next RNN cell at stage $k+1$.

b) Loss Computation.: Because the objective (6) involves both state costs $C_1(\omega)$ (e.g., L^2 or L_∞ norms of frequency deviation) and action costs $C_2(u)$ (e.g., quadratic penalty on u or renewable-curtailment costs), we evaluate them at each

Algorithm 1: Reinforcement Learning to train the control function with RNN unrolling

Input: Learning rate α, batch size H, total time stages K, number of episodes N.

Output: Optimized neural network weights Θ for control

Initialization: Randomly initialize weights Θ of the neural network controller (26)
for *episode = 1 to* N **do** `// outer loop`
  for $h = 1$ *to* H **do** `// mini-batch loop`
    `// (1) Randomly sample initial load step`
    Generate random initial load change Δp_m within the specified bounds for bus $i = 1, \ldots, n$.
    `// (2) Roll out the unrolled RNN through` K `stages`
    for $k = 0$ *to* $K - 1$ **do**
      (a) Pass $(\theta_i^h(k), \omega_i^h(k))$ through the RNN cell (which implements (26) internally) to obtain the control action $u_i^h(k)$
      (b) Simulate one step of the power system dynamics (7) with time step Δt to get $(\theta_i^h(k+1), \omega_i^h(k+1))$
    end
    `// (3) Compute the cost of the trajectory`
    Use the objective in (6).
  end
  `// (4) Aggregate losses and update neural network`
  $\text{TotalLoss} = \frac{1}{H}\sum_{h=1}^{H} \text{Loss}_h$
  (a) Perform backpropagation through the unrolled RNN layers (including the non-monotonic design (26) and parameter clipping)
  (b) Update $\Theta \leftarrow \Theta - \alpha\, \nabla_\Theta(\text{TotalLoss})$ using Adam or a similar optimizer
end

time step and sum (or take the max) over the entire horizon $0, \ldots, K$. Concretely,

$$\text{TotalLoss} \;=\; \tfrac{1}{H}\sum_{h=1}^{H}\sum_{i=1}^{n} \underbrace{C_1\big(\omega_i^h(k)_{k=0}^{K}\big)}_{\text{state cost}} + \gamma\, C_2\big(u_i^h(k)_{k=0}^{K}\big),$$

where $h \in \{1, \cdots, H\}$ indexes the mini-batches (each simulating a distinct trajectory with different initial states or load disturbances).

c) Backward Pass (Gradient and Parameter Updates).: To train the network weights Θ (including the clipping for α_i), we use backpropagation through time (BPTT). Specifically, automatic differentiation frameworks compute the gradient of the loss by unrolling the RNN for K steps and chaining derivatives of each cell's outputs with respect to the previous cell's states and actions. Overall, this RNN-based scheme provides a direct way to optimize closed-loop policies $u_i(\omega_i)$ by simulating realistic power-system trajectories. Once trained, the neural controller can be deployed in real time: at each sampling instant, measure the local frequency ω_i, feed it into the trained network, and apply the computed $u_i(\omega_i)$ to the inverter.

VI. Experiments

To validate the claim of our method, we use the IEEE-39 New England test system, commonly used for stability analysis [21], [50]. This is because the New England system has been designed to emulate the dynamic response of medium-sized power networks [51]. In this test case, there are 10-connected generators, and it is assumed that for each generator, there is a connected renewable inverter to act as the controller. To validate our method, we compare it with respect to past methods. We also conduct such comparisons for various types of cost functions and different load disturbances to check the generalizability claimed in the earlier sections.

A. Simulation Setup

For the simulation setup, the training is done using the Keras Tensorflow framework with Nvidia 3070 GPU. The dynamic response of the network is modeled using ANDES, an open-source Python package for power system dynamic simulation [52], where a 6^{th} order model is used for the generators and Western Electricity Coordinating Council (WECC) models for the inverter resources. For benchmarking, we use different combinations of traditional generations and inverter-based generations on different buses. Once the load is chosen, we assume the load to be constant during the operation, which is typical for short-scale primary frequency control analysis [30].

To train the network, we generate 800 batches of 2 seconds trajectories with uniform load and generation step change between $[-1, 1]$ p.u. Training is carried out for 200 epochs to ensure convergence. We evaluate performance using L^2- and L_∞-norms for state loss, while action loss is assessed through different combinations of metrics, including degradation, emissions, and fuel savings, each with adjustable weights. For validating our contribution on a larger feasibility region, we consider the same setup with the monotonic ReLU design in [23]. For example, we train the same neural network to minimize the same cost with L^∞-norm for the state cost, where $\gamma = 0.005$, $\beta = 0.002$, and $\alpha = 0.6$. For benchmark methods, we use Monotonic-ReLU [23] as the nominal benchmark, but we include two additional benchmarks representing primary methods of optimal frequency control. First, policy search based unconstrained optimization where (5) is solved with an optimization solver with linear parametrization [9] which we refer to as Optimal-Linear. The second is learning based approach where the Lyapunov function is learned instead of guaranteeing the stability by design [21], [48], which we will refer to as Learned-Lyapunov.

B. Feasible Region Comparison

Fig. 3 shows the optimized activation function for controllers when $\gamma = 0.005$ in optimization (6), where γ is the

weight for the two metrics in the objective function. The x-axis is the measured frequency deviation, and the y-axis is the corresponding inverter action. The subplots of Fig. 3 are for buses 30, 31, 32, and 33 when the optimization achieves the optimal results. The selected buses are at different edges for representative illustration. In the figure, we first show the original region from the past method [23] in purple. Our approach enlarges the region to include the region in pink. As we can see, the pink region is significant, so our approach explores both the purple and pink regions freely. Then, we present the optimization results from the past method and the proposed method. The dashed blue line is from the past method. It stays strictly within the blue region. Our proposed control method has more freedom, and the optimized control rule in the red line can happen in both purple and pink regions. For example, the control rule can be in the same regions or different regions (i.e., bottom right sub-plot in Fig. 2). A unique feature is that our design allows a non-monotonic control function, which helps achieve optimal results. This non-monotonicity allows the inverter to either increase its generation in the under-frequency case when the frequency deviation is below a certain threshold, then increase it when it rises above that, such as the top right subplot, or be monotonically decreasing as the bottom right subplot. This gives flexibility in the inverter operation to do what is optimal based on the given objective.

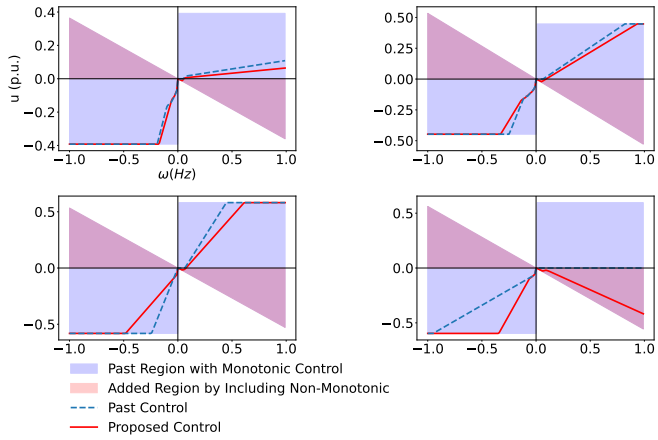

Figure 2: Control function for monotonic and non-monotonic design for the four inverters at buses $30, 31, 32$, and 33 for $\gamma = 0.005$.

For validation on diverse values of γ, we increase γ from 0.005 to 0.008 shown in Fig. 3. The goal is to check our results when giving more weight to the action penalty. We observe that the two regions are the same, but the optimized control rules have different behaviors. In particular, our proposed method can stay in the pink region with non-monotonic properties. For example, the last figure shows that the past methods tries to be close to the pink region in our proposed method. Our method can go beyond the boundary between the purple and pink regions for better optimality. We observe from the Fig. 3 that for the first, second, and fourth sub-plots, the inverters prioritize increasing renewable generation in the over-frequency scenario. In the under-frequency scenario for the third sub-plot, both controllers are monotonic as they both increase renewable generation in such case.

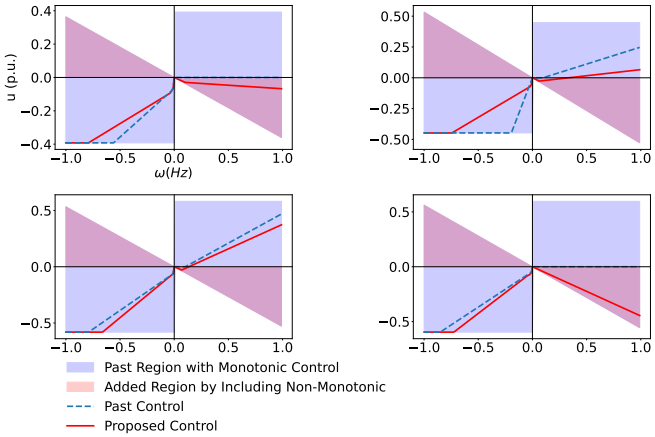

Figure 3: Control function for monotonic and non-monotonic design for the four inverters at buses $30, 31, 32$, and 33 for $\gamma = 0.008$.

C. Objective Comparison During Training

In addition to comparing how much we improve the feasible region, it is critical to quantify how much improvement our method gives on the objective. Therefore, we use Fig. 4 to show how the performance comparison between the past method with a monotonic function [23] in blue dashed line and the proposed method in solid red line. The x-coordinate shows the epochs during training, and the y-coordinate shows the total loss in the objective. We can see that the performances are similar at the beginning. However, the red one gradually outperforms in the sense of having a lower loss after 25 epochs. The losses for both methods stabilize after 100 iterations. The final loss is -0.8 for the old method in blue and -1.1 for the proposed method in red. And, the improvement is about 37%.

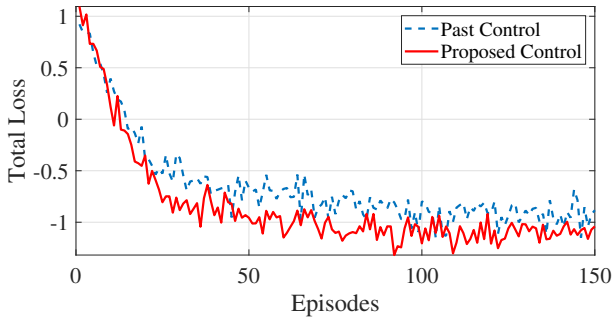

Figure 4: Convergence comparison for the proposed and the Monotonic-ReLU method.

D. Performance Comparison with Different Objective Designs

After showing how the proposed method improves its performance during the training process, we will show the

This article has been accepted for publication in IEEE Transactions on Power Systems. This is the author's version which has not been fully edited and content may change prior to final publication. Citation information: DOI 10.1109/TPWRS.2025.3597567

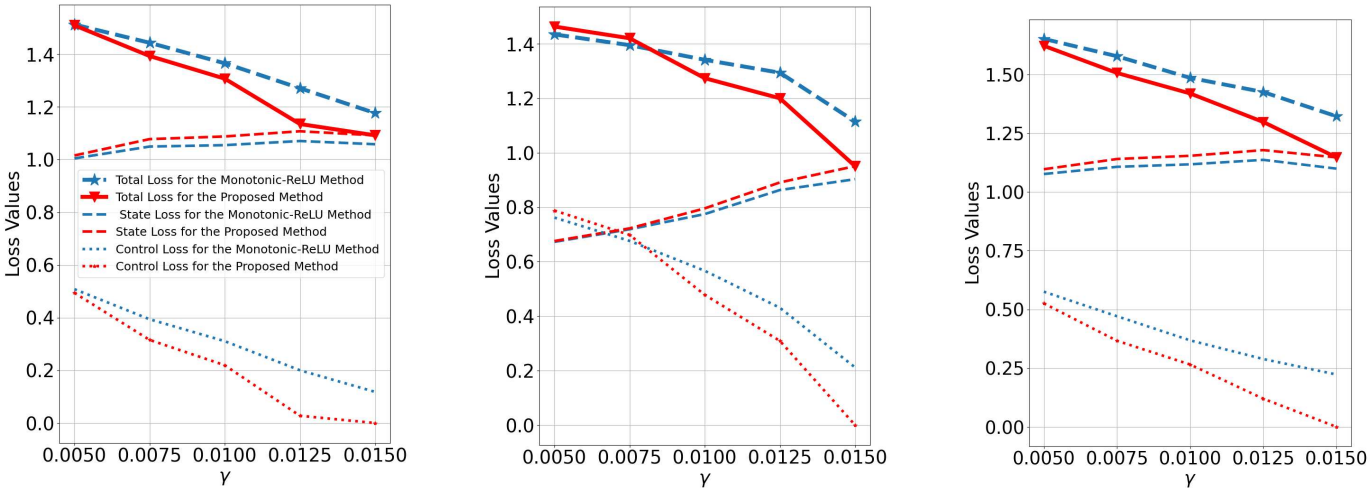

(a) L^2 Loss. (b) L_∞ Loss. (c) L_∞ with RoCoF.

Figure 5: Total costs, state costs, and action cost for the past and proposed control methods as the weight γ changes.

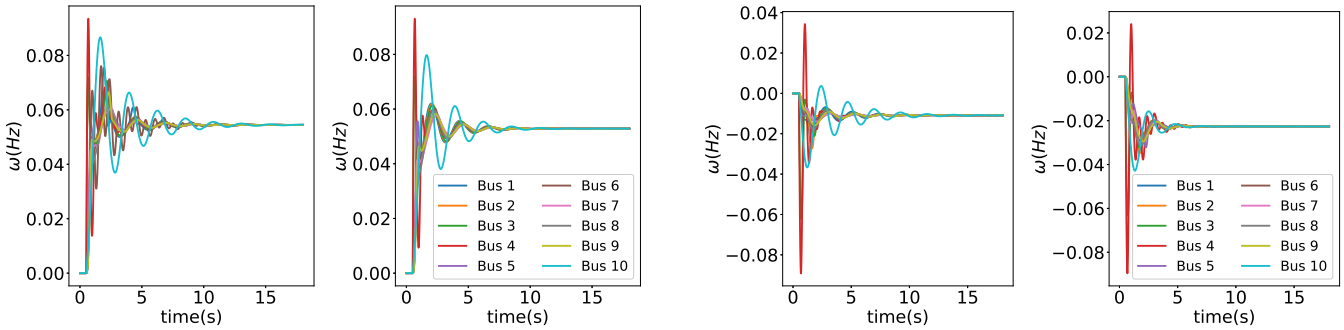

(a) Over frequency with 1 p.u. step load decrease. (b) Under frequency with 1 p.u. step load increase.

Figure 6: Frequency response of the proposed controller in comparison to the monotonic ReLU controller in both over frequency and under frequency events with high disturbance. In both subplots, the proposed controller is on the left and the monotonic is on the right.

converged results with different objective functions and different weights. For example, Fig. 7a illustrates the total cost, average state, and action costs with the same setup as the last subsection. In such a setup, we have an L_2 norm on frequency deviation for C_1. Similarly, we consider the step load change analysis by various values of γ. The x-axis of Fig. 5 is the action penalty γ, and the y-axis is the cost function. We draw six lines in the figure, as we not only compare the total costs but also their sub-components on state costs and control costs. We can see that the proposed method not only has a lower total cost but also reduces the action cost significantly.

We change the objective to convert L_2 to L_∞ norm in Fig. 7b. We also include RoCoF in Fig. 5c to reflect the Rate of Change of Frequency (RoCoF). In both figures, we can observe the same phenomenon that our proposed method can reduce the total cost. Also, the larger the γ infers more control cost and better overall performance. In Fig. 7b and Fig. 5c, we observe improvement in the action cost due to increased renewable generation with a slight increase in the state cost, and the tradeoff is controlled by the value of γ. This shows that having a non-monotonic response for the inverter controller design can still stabilize the system and minimize all forms of frequency loss metrics as long as the coordinated response remains monotonic. For the subsequent simulations, the proposed controller adopts the design in 5c with $\gamma = 0.005$, combining the penalty on maximum frequency deviation and RoCoF.

E. Significant Performance for Boosting Renewable Energy

Last subsection shows that our approach can boost renewable.

So, Fig. 9 looks into the net change of renewable curtailment over time, when there is a step load decreases of 10% on buses 30, 31, and 32 at $t = 0.5$. Specifically, Fig. 9 shows the total power produced by all buses' inverters in both proposed and monotonic designs. The blue and red lines are the same initially. After the load change, the red line stays higher than the blue line. This shows that our proposed design increases renewable production in the transient and reduces steady-state curtailment, which agrees with the coordination

This article has been accepted for publication in IEEE Transactions on Power Systems. This is the author's version which has not been fully edited and content may change prior to final publication. Citation information: DOI 10.1109/TPWRS.2025.3597567

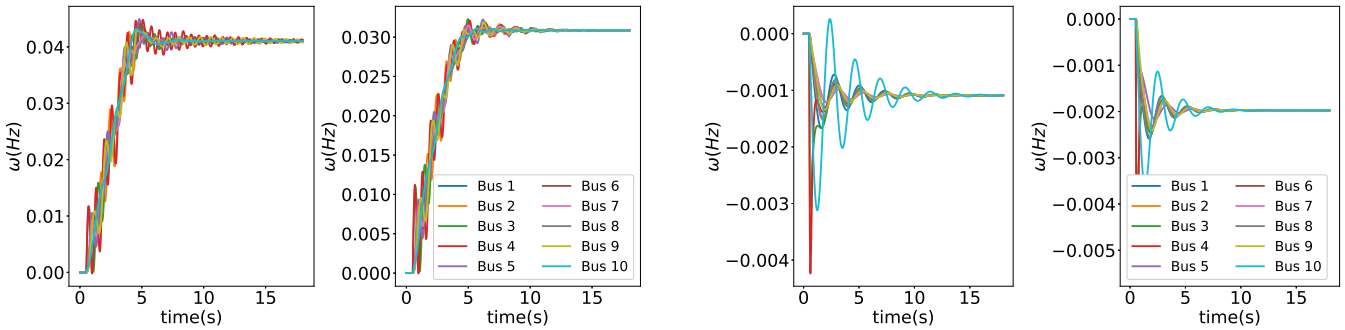

(a) Over frequency with 0.1 p.u. step load decrease .

(b) Under frequency with 0.1 p.u. step load increase.

Figure 7: Frequency response of the proposed controller in comparison to the monotonic ReLU controller in both over frequency and under frequency events with low disturbance. In both subplots, the proposed controller is on the left and the monotonic is on the right.

expected from our non-monotonic design. We examine the response further by looking at all the inverters generation in Fig. 8 for both the proposed and monotonic designs and observe. Unlike the past control, The proposed design let some inverters increase their generation during the over frequency where the generation is sufficient from synchronous generators. For example, we observe in Fig. 8 that some inverters can increase their generation even during a load decrease due to the expanded region. Finally, we validate the frequency stability in Fig. 10, which shows that the proposed method maintains frequency stability below 0.05 HZ while minimizing curtailment, while the Learned-Lyapunov method sacrifices exhibits a much larger deviation.

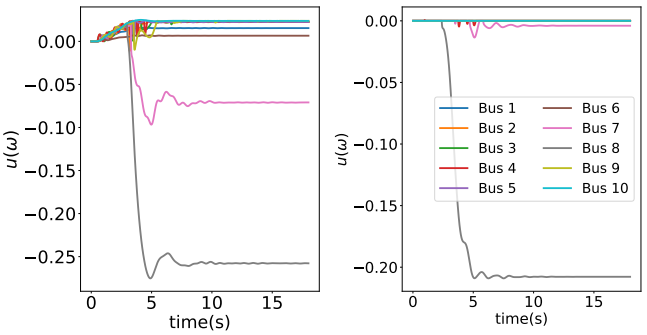

Figure 8: (a) Inverter generation offset for proposed design (b) Inverter generation offset for monotonic ReLU design.

F. Evaluate Transient System Stability

The previous sections show that our method works better than the past in the sense of lower objectives and the capability to boost renewable. However, it is critical to make sure that all the constraints are satisfied. For example, a critical constraint motivating this paper comes from the Lyapunov stability. For thoroughness, we show the stability performance with both under-frequency and over-frequency cases at different disturbance levels. First for high disturbance, the step load is decreased by 1 p.u. at $t = 0.5s$, while for the under frequency the load is increased by 1 p.u. shown in figure Fig 6. The figures depict the evolution of the system's frequency during the disturbance. We observe that despite the sudden disturbance, the frequencies on all buses converge to a common value, indicating that synchronism is maintained. Moreover, we observe that both the proposed design and monotonic-ReLU achieve a similar maximum frequency deviation of around 0.09 Hz. This validates that the renewable curtailment minimization does diminish the frequency response to large deviations. On the other hand, the curtailment minimization is evidence during the smaller disturbance, which we simulate with a load change of 0.1 p.u. as in Fig. 7. We observe that the proposed method exhibits a larger frequency deviation; however, it is within 0.04 Hz, which is within safe operating conditions.

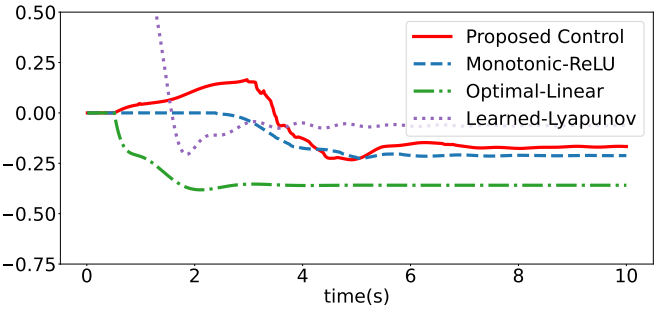

Figure 9: The total power produced by all buses' inverters by the proposed design and benchmark methods.

G. Robustness Evaluation via Sensitivity Analysis on Disturbances and Costs

For robustness evaluation, we test with a wide range of scenarios in Figs 11 and 12. For example, we test various disturbance events. We also randomly select three generators for each event, and we vary the step load change at those buses between -1 p.u. to 1 p.u., and the simulation is repeated over 50 iterations per step load change. This setup ensures a

This article has been accepted for publication in IEEE Transactions on Power Systems. This is the author's version which has not been fully edited and content may change prior to final publication. Citation information: DOI 10.1109/TPWRS.2025.3597567

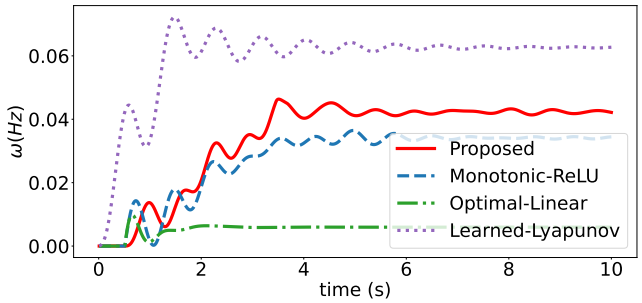

Figure 10: The maximum frequency deviation in all buses under the proposed design and benchmark methods.

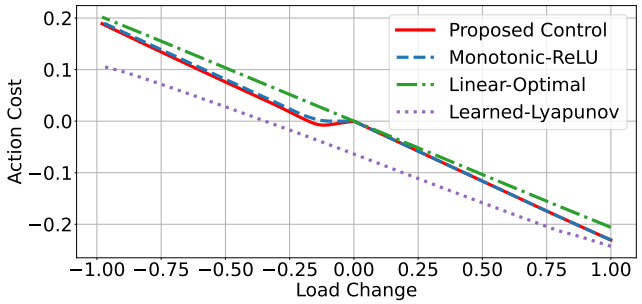

Figure 12: Change of inverter generation loss within a range of step load changes for the proposed Lyapunov controller and the benchmark methods.

comprehensive comparison of our proposed method for a wide range of events. Fig. 11 shows the average performance of the frequency cost on the y coordinate against the load change on the x coordinate. Also, Fig. 12 shows the average performance of the renewable generation loss cost on the y coordinate against the load change on the x coordinate. From the figures, we observe that under-load scenarios have a trade-off between the renewable curtailment cost and frequency deviation cost, and the non-monotonic design yields better performance, e.g., significantly lower cost. The improvement is most apparent in the $[-.25, 0]$ range where the proposed method has an average 15% decrease in net curtailment over the Monotonic-ReLU and a maximum improvement of 50% when the step load changes by 6%. Moreover, the proposed method has a consistent cost decrease over linear. The learned-Lyapunov method achieves a lower action cost but fails to maintain frequency safety, as it is missing the theoretical guarantee we provide. Finally, as the improvement occurs in low deviation events, which are more prominent, it will accumulate consistently over time, leading to significant savings. In Fig. 13, we can see the cost improvement of the proposed method. On the other hand, our cost is almost identical to that of the monotonic design in the overload scenario. This is because both the monotonic and non-monotonic designs increase the generation during an overload event.

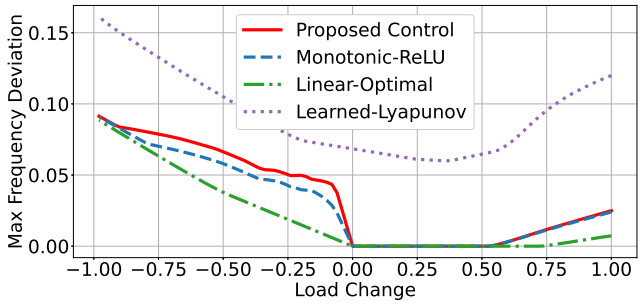

Figure 11: Change of maximum frequency within a range of step load changes for the proposed Lyapunov controller and the benchmark methods.

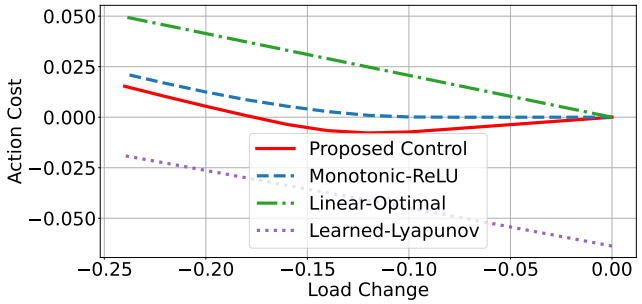

Figure 13: Change of inverter generation loss within over frequency low disturbance events for the proposed Lyapunov controller and the benchmark methods.

VII. Conclusion

This paper proposes to enlarge the feasibility region for optimizing primary frequency control. The extended region is rigorously proved to be sufficiently large to contain a globally optimal solution, but the past region usually doesn't contain such a solution. As a consequence, our proposed Lyapunov neural controller shows better performance than the past methods. The better performance is due to our design of using the damping resources to expand the Lyapunov stable policies in the neural network's search space. Based on the property of the control, we design a non-monotonic ReLU function for action exploration. As the new design allows the optimization of a wider range of cost functions, we show that we can have better renewable curtailment and lower fuel costs, which the monotonic design fails to optimize.

References

[1] United Nations Framework Convention on Climate Change (UNFCCC), "Nationally determined contributions under the paris agreement. synthesis report by the secretariat," 2021.

[2] H. Li, Y. Weng, E. Farantatos, and M. Patel, "A hybrid machine learning framework for enhancing pmu-based event identification with limited labels," in *2019 International Conference on Smart Grid Synchronized Measurements and Analytics (SGSMA)*, 2019, pp. 1–8.

[3] ——, "An unsupervised learning framework for event detection, type identification and localization using pmus without any historical labels," in *2019 IEEE Power Energy Society General Meeting (PESGM)*, 2019, pp. 1–5.

[4] H. Li, Z. Ma, and Y. Weng, "A transfer learning framework for power system event identification," *IEEE Transactions on Power Systems*, vol. 37, no. 6, pp. 4424–4435, 2022.

[5] H. Li, Z. Ma, Y. Weng, E. Blasch, and S. Santoso, "Structural tensor learning for event identification with limited labels," *IEEE Transactions on Power Systems*, vol. 38, no. 6, pp. 5314–5328, 2023.

[6] Z. Zhang, E. Du, F. Teng, N. Zhang, and C. Kang, "Modeling frequency dynamics in unit commitment with a high share of renewable energy," *IEEE Transactions on Power Systems*, vol. 35, no. 6, pp. 4383–4395, 2020.

[7] Y. Zhang and L. Xie, "A transient stability assessment framework in power electronic-interfaced distribution systems," *IEEE Transactions on Power Systems*, vol. 31, no. 6, pp. 5106–5114, 2016.

[8] B. K. Poolla, S. Bolognani, and F. Dörfler, "Optimal placement of virtual inertia in power grids," *IEEE Transactions on Automatic Control*, vol. 62, no. 12, pp. 6209–6220, 2017.

[9] Z. Zhang, E. Du, F. Teng, N. Zhang, and C. Kang, "Modeling frequency dynamics in unit commitment with a high share of renewable energy," *IEEE Transactions on Power Systems*, vol. 35, no. 6, pp. 4383–4395, 2020.

[10] A. Ademola-Idowu and B. Zhang, "Frequency stability using mpc-based inverter power control in low-inertia power systems," *IEEE Transactions on Power Systems*, vol. 36, no. 2, pp. 1628–1637, 2021.

[11] M. J. Rahman, T. Tafticht, M. L. Doumbia, and I. Messaïf, "Optimal inverter control strategies for a pv power generation with battery storage system in microgrid," *Energies*, vol. 16, no. 10, 2023.

[12] Y.-K. Wu, W.-H. Yang, Y.-L. Hu, and P. Q. Dzung, "Frequency regulation at a wind farm using time-varying inertia and droop controls," *IEEE Transactions on Industry Applications*, vol. 55, no. 1, pp. 213–224, 2019.

[13] M. Fakhari Moghaddam Arani and Y. A.-R. I. Mohamed, "Dynamic droop control for wind turbines participating in primary frequency regulation in microgrids," *IEEE Transactions on Smart Grid*, vol. 9, no. 6, pp. 5742–5751, 2018.

[14] A. Naderipour, Z. Abdul-Malek, I. F. Davoodkhani, H. Kamyab, and R. R. Ali, "Load-frequency control in an islanded microgrid pv/wt/fc/ess using an optimal self-tuning fractional-order fuzzy controller," *Environmental Science and Pollution Research*, vol. 30, no. 28, pp. 71 677–71 688, 2023.

[15] B. Kiumarsi, K. G. Vamvoudakis, H. Modares, and F. L. Lewis, "Optimal and autonomous control using reinforcement learning: A survey," *IEEE Transactions on Neural Networks and Learning Systems*, vol. 29, no. 6, pp. 2042–2062, 2018.

[16] Y. Chow, O. Nachum, E. Duenez-Guzman, and M. Ghavamzadeh, "A lyapunov-based approach to safe reinforcement learning," in *Proceedings of the 32nd International Conference on Neural Information Processing Systems*, ser. NIPS. Red Hook, NY, USA: Curran Associates Inc., 2018, p. 8103–8112.

[17] H. Li, Y. Weng, and H. Tong, "Console: Convex neural symbolic learning," in *Advances in Neural Information Processing Systems*, S. Koyejo, S. Mohamed, A. Agarwal, D. Belgrave, K. Cho, and A. Oh, Eds., vol. 35. Curran Associates, Inc., 2022, pp. 5766–5774.

[18] Q. Gan, F. Wu, and J. Zhao, "A survey of research on stability guarantee of reinforcement learning automatic control problem," in *2021 6th International Conference on Control, Robotics and Cybernetics (CRC)*, 2021, pp. 240–249.

[19] H. Alduaij, B. Zhang, and Y. Weng, "Determining feasibility of dc power flow using graph neural networks," in *2024 IEEE Power Energy Society General Meeting (PESGM)*, 2024, pp. 1–5.

[20] I. M. Ross and F. Fahroo, "Issues in the real-time computation of optimal control," *Mathematical and Computer Modelling*, vol. 43, no. 9, pp. 1172–1188, 2006, optimization and Control for Military Applications.

[21] T. Zhao, J. Wang, X. Lu, and Y. Du, "Neural lyapunov control for power system transient stability: A deep learning-based approach," *IEEE Transactions on Power Systems*, vol. 37, no. 2, pp. 955–966, 2022.

[22] H. Alduaij and Y. Weng, "Online voltage regulation with minimum disturbance for distribution grid without system knowledge," *IEEE Open Access Journal of Power and Energy*, vol. 11, pp. 520–531, 2024.

[23] W. Cui, Y. Jiang, and B. Zhang, "Reinforcement learning for optimal primary frequency control: A lyapunov approach," *IEEE Transactions on Power Systems*, pp. 1–1, 2022.

[24] Z. Yuan, C. Zhao, and J. Cortés, "Reinforcement learning for distributed transient frequency control with stability and safety guarantees," *Systems & Control Letters*, vol. 185, p. 105753, 2024.

[25] Y. Jiang, W. Cui, B. Zhang, and J. Cortés, "Stable reinforcement learning for optimal frequency control: A distributed averaging-based integral approach," *IEEE Open Journal of Control Systems*, vol. 1, pp. 194–209, 2022.

[26] P. Kundur, "Power system stability," *Power system stability and control*, vol. 10, pp. 7–1, 2007.

[27] H. Li and Y. Weng, "Physical equation discovery using physics-consistent neural network (pcnn) under incomplete observability," in *Proceedings of the 27th ACM SIGKDD Conference on Knowledge Discovery & Data Mining*, ser. KDD '21. New York, NY, USA: Association for Computing Machinery, 2021, p. 925–933.

[28] H. Li, Y. Weng, V. Vittal, and E. Blasch, "Distribution grid topology and parameter estimation using deep-shallow neural network with physical consistency," *IEEE Transactions on Smart Grid*, vol. 15, no. 1, pp. 655–666, 2024.

[29] B. Zhang, J. Jin, C. Fang, and L. Wang, "Improved analysis of clipping algorithms for non-convex optimization," *Advances in Neural Information Processing Systems*, vol. 33, pp. 15 511–15 521, 2020.

[30] P. Kundur, *Power system stability and control*. McGraw-hill New York, 1994.

[31] C. Zhao, U. Topcu, N. Li, and S. Low, "Design and stability of load-side primary frequency control in power systems," *IEEE Transactions on Automatic Control*, vol. 59, no. 5, pp. 1177–1189, 2014.

[32] E. Weitenberg, Y. Jiang, C. Zhao, E. Mallada, C. De Persis, and F. Dörfler, "Robust decentralized secondary frequency control in power systems: Merits and tradeoffs," *IEEE Transactions on Automatic Control*, vol. 64, no. 10, pp. 3967–3982, 2019.

[33] C. Dawson, S. Gao, and C. Fan, "Safe control with learned certificates: A survey of neural lyapunov, barrier, and contraction methods," 2022.

[34] Y. Chow, O. Nachum, E. Duenez-Guzman, and M. Ghavamzadeh, "A lyapunov-based approach to safe reinforcement learning," *Advances in neural information processing systems*, vol. 31, 2018.

[35] E. Todorov, "268269Optimal Control Theory," in *Bayesian Brain: Probabilistic Approaches to Neural Coding*. The MIT Press, 12 2006.

[36] S. Panda and N. K. Yegireddy, "Automatic generation control of multi-area power system using multi-objective non-dominated sorting genetic algorithm-ii," *International Journal of Electrical Power & Energy Systems*, vol. 53, pp. 54–63, 2013.

[37] N. Rezaei and M. Kalantar, "Economic–environmental hierarchical frequency management of a droop-controlled islanded microgrid," *Energy conversion and management*, vol. 88, pp. 498–515, 2014.

[38] M. Ramírez, R. Castellanos, G. Calderón, and O. Malik, "Placement and sizing of battery energy storage for primary frequency control in an isolated section of the mexican power system," *Electric Power Systems Research*, vol. 160, pp. 142–150, 2018.

[39] P. Astero, S. H. Hosseinian, and M. Abedi, "A novel multi-stage fuel cost minimization in a vsc-based microgrid considering stability, frequency, and voltage constraints," *IEEE Transactions on Power Systems*, vol. 28, no. 2, pp. 931–939, 2013.

[40] M.-T. Kuo, S.-D. Lu, and M.-C. Tsou, "Considering carbon emissions in economic dispatch planning for isolated power systems: A case study of the taiwan power system," *IEEE Transactions on Industry Applications*, vol. 54, no. 2, pp. 987–997, 2017.

[41] A. Varshney, R. Loka, and A. M. Parimi, "Fast frequency response using model predictive control for a hybrid power system," in *2021 IEEE 9th International Conference on Smart Energy Grid Engineering (SEGE)*, 2021, pp. 104–110.

[42] P. W. Sauer, M. A. Pai, and J. H. Chow, *Power system dynamics and stability: with synchrophasor measurement and power system toolbox*. John Wiley & Sons, 2017.

[43] E. Weitenberg, Y. Jiang, C. Zhao, E. Mallada, C. De Persis, and F. Dörfler, "Robust decentralized secondary frequency control in power systems: Merits and tradeoffs," *IEEE Transactions on Automatic Control*, vol. 64, no. 10, pp. 3967–3982, 2018.

[44] K. E. Martin, G. Benmouyal, M. Adamiak, M. Begovic, R. Burnett, K. Carr, A. Cobb, J. Kusters, S. Horowitz, G. Jensen *et al.*, "Ieee standard for synchrophasors for power systems," *IEEE Transactions on Power Delivery*, vol. 13, no. 1, pp. 73–77, 1998.

[45] E. Weitenberg, Y. Jiang, C. Zhao, E. Mallada, C. De Persis, and F. Dörfler, "Robust decentralized secondary frequency control in power systems: Merits and tradeoffs," *IEEE Transactions on Automatic Control*, vol. 64, no. 10, pp. 3967–3982, 2019.

[46] *Energy Function Methods*. John Wiley & Sons, Ltd, 2017, ch. 9, pp. 233–261.

[47] R. M. Wright, "Understanding modern generator control," *IEEE Power Engineering Review*, vol. 9, no. 9, pp. 46–46, 1989.

[48] W. Cui and B. Zhang, "Lyapunov-regularized reinforcement learning for power system transient stability," *IEEE Control Systems Letters*, vol. 6, pp. 974–979, 2022.

[49] D. E. Kirk, *Optimal control theory: an introduction*. Courier Corporation, 2004.
[50] M. Liu, I. Dassios, G. Tzounas, and F. Milano, "Model-independent derivative control delay compensation methods for power systems," *Energies 2020, Vol. 13, Page 342*, vol. 13, p. 342, 1 2020.
[51] T. Athay, R. Podmore, and S. Virmani, "A practical method for the direct analysis of transient stability," *IEEE Transactions on Power Apparatus and Systems*, vol. PAS-98, no. 2, pp. 573–584, 1979.
[52] H. Cui and F. Li, "Andes: A python-based cyber-physical power system simulation tool," in *North American Power Symposium (NAPS)*, 2018, pp. 1–6.